

# The origin of double-peaked narrow emission-line galaxies in MaNGA Survey

Zhiyun Zhang<sup>1,2,3</sup> , Yanmei Chen<sup>1,2,3</sup> , Shiyin Shen<sup>4,5</sup> , Guinevere Kauffmann<sup>6</sup>, Min Bao<sup>1,2,3</sup> ,  
Zhijie Zhou<sup>1,2,3</sup> , Gaoxiang Jin<sup>6</sup>  and Yuren Zhou<sup>1,2,3</sup> 

<sup>1</sup>*School of Astronomy and Space Science, Nanjing University, Nanjing 210093, China*

<sup>2</sup>*Key Laboratory of Modern Astronomy and Astrophysics (Nanjing University), Ministry of Education, Nanjing 210093, China*

<sup>3</sup>*Collaborative Innovation Center of Modern Astronomy and Space Exploration, Nanjing 210093, China*

<sup>4</sup>*Shanghai Astronomical Observatory, Chinese Academy of Sciences, 80 Nandan Road, Shanghai 200030, China*

<sup>5</sup>*Key Lab for Astrophysics, Shanghai 200034, China*

<sup>6</sup>*Max Planck Institute for Astrophysics, Karl-Schwarzschild-Str. 1, D-85741 Garching, Germany*

Accepted XXX. Received YYY; in original form ZZZ

## ABSTRACT

We select 36 double-peaked narrow emission-line galaxies (DPGs) from 10,010 unique galaxies in MaNGA survey. These DPGs show double-peaked Balmer lines and forbidden lines in the spectra. We use a double Gaussian model to separate the double-peaked profiles of each emission line into blue and red components ( $\lambda_{\text{blue}} < \lambda_{\text{red}}$ ), and analyze the spatially resolved kinematics and ionization mechanisms of each component. We find that in 35 out of 36 DPGs, the flux ratio between the blue and red components varies systematically along the major axes, while it keeps roughly a constant along the minor axes. The blue and red components of these DPGs exhibit similar distributions in both the value of line-of-sight velocity and the velocity dispersion. Additionally, 83.3% DPGs have both blue and red components located in the same ionization region in the [S II]-BPT diagram. Combining all these observational results, we suggest that the double-peaked emission line profiles in these 35 DPGs primarily originate from rotating discs. The remaining one galaxy shows clear outflow features. 8 out of 35 DPGs show symmetric line profiles that indicate undisturbed rotating discs, and the other 27 DPGs exhibit asymmetric profiles, suggesting dynamic disturbances in the rotating discs. Furthermore, we find that 58.3% DPGs experienced external processes, characterized by tidal features, companion galaxies, as well as gas-star misalignments. This fraction is about twice as much as that of the control sample, suggesting the origin of double-peaked emission line profiles is associated with external processes.

**Key words:** galaxies: evolution – galaxies: kinematics and dynamics – galaxies: interactions.

## 1 INTRODUCTION

The emission-line spectra of galaxies contain a wealth of physical information for the ionized gas, such as kinematics and ionization mechanisms (Kewley et al. 2019). Typically, emission lines in galaxy spectra are described by a single Gaussian or Lorentzian profile. Double-peaked emission line profiles were discovered in several individual objects in early narrow-line region (NLR) studies (e.g. Mrk 78, 3C 305 and NGC 4151; Sargent 1972; Heckman et al. 1981, 1984), suggesting the presence of two distinct gas components with different line-of-sight velocities.

In the past 15 years, systematic searches for kiloparsec-scale dual AGNs have focused on galaxies with double-peaked narrow emission lines. Using the spatially integrated spectra, Wang et al. (2009), Liu et al. (2010), and Smith et al. (2010) selected double-peaked AGN samples from Data Release 7 of the Sloan Digital Sky Survey (SDSS DR7; Abazajian et al. 2009), which in total contain 340 AGNs with double-peaked [O III] $\lambda 5007$  emission line profiles. However, in

follow-up multi-band photometric and spectroscopic observations of these objects, only a small fraction of them have been confirmed as dual AGNs through high-resolution radio, X-ray and/or infrared imaging, as well as integral-field spectroscopy. For 18 double-peaked AGNs with FIRST detections and optical long-slit spectra that exhibit two relatively compact AGN emission components with angular separations of  $\geq 0.2$  arcsec, Müller-Sánchez et al. (2015) found that  $\sim 17\%$  (3/18) galaxies show two spatially separated radio cores in high-resolution multi-band Very Large Array (VLA) images, suggesting these three galaxies as dual AGNs. Comerford et al. (2015) used high-resolution *HST* and *Chandra* observations to investigate 12 galaxies in which the long-slit spectroscopy shows two [O III] $\lambda 5007$  components separated by  $\geq 0.75$  arcsec (Greene et al. 2011; Shen et al. 2011; Comerford et al. 2012). They confirmed one dual AGN system where the two stellar bulges have coincident [O III] $\lambda 5007$  and X-ray counterparts, corresponding to  $\sim 8\%$  (1/12) of the sample. Moreover, Fu et al. (2012) investigated 106 double-peaked narrow emission line galaxies using high-resolution Keck/*HST* images or integral-field spectroscopy (IFS) data, suggesting  $\sim 2\%$  (2/106) of these galaxies are dual AGNs. The double-peaked profiles of these

\* E-mail: chenym@nju.edu.cn

two objects are driven by the orbital motion of merging galaxies, with two concentrated  $[\text{O III}]\lambda\lambda 5007$  components spatially coincident with two stellar nuclei.

Considering that the majority of double-peaked AGNs are not expected to be dual AGNs, other mechanisms such as rotating discs and inflows/outflows have been proposed by several studies to explain the origin of double-peaked emission line profiles (Greene & Ho 2005; Shen et al. 2011; Smith et al. 2012; Fu et al. 2012; Müller-Sánchez et al. 2015; Nevin et al. 2016; Diniz et al. 2017; Nevin et al. 2018; Comerford et al. 2018; Benedetti et al. 2024). For example, Müller-Sánchez et al. (2015) found that the double-peaked profiles in  $\sim 72\%$  (13/18) galaxies are produced by rotating discs or outflows. They identified radio jet-driven outflows in 5 out of 13 galaxies based on extended radio emission and alignment of the radio jet with the ionized gas. Additionally, 7 out of 13 galaxies were classified as AGN wind-driven outflows primarily due to significant misalignment ( $> 15^\circ$ ) between the position angle of the two  $[\text{O III}]\lambda\lambda 5007$  emission components and the photometric major axis of the galaxy. The remaining 1 out of 13 galaxies was classified as a rotating disc, with the two  $[\text{O III}]\lambda\lambda 5007$  emission components spatially coincident with the galaxy's photometric major axis. In a follow-up study based on the same parent sample of 340 double-peaked AGNs, Nevin et al. (2016) used optical long-slit observations to systematically classify 71 double-peaked Type 2 AGNs at  $z < 0.1$  into outflow-dominated and rotation-dominated categories. As a result,  $\sim 86\%$  (61/71) galaxies with broad wing components were classified as outflow-dominated. In contrast,  $\sim 6\%$  (4/71) galaxies were classified as rotation-dominated. In these rotation-dominated galaxies, the  $[\text{O III}]\lambda\lambda 5007$  spectrum shows two narrow components, which are located along the photometric major axis of the galaxy. The remaining  $\sim 8\%$  (6/71) were classified as "Ambiguous", with two narrow components, which are not aligned with the photometric major axis of the galaxy.

However, long-slit spectroscopy has limited spatial coverage, resulting in the loss of spatial information when analyzing spatially extended structures. Comparing to the long-slit spectroscopy, integral-field spectroscopy provides more complete spatial coverage and is thus crucial for investigating the nature of double-peaked narrow emission-line galaxies. With the complete release of the Mapping Nearby Galaxies at Apache Point Observatory (MaNGA; Bundy et al. 2015) integral field unit (IFU) survey, several works have tried to explore the origin of double-peaked emission line profiles using IFU data, including case studies (Wang et al. 2019; Mazzilli Ciraulo et al. 2021) and sample-based statistical studies (Fu et al. 2023; Qiu et al. 2024, 2025). From  $\sim 10,000$  galaxies in the final data release of MaNGA, Fu et al. (2023) identified 188 galaxies with emission lines that cannot be described by a single Gaussian component. Among them, 49 galaxies exhibit double-peaked profiles in both the Balmer lines (e.g.  $\text{H}\alpha$ ) and forbidden lines (e.g.  $[\text{O III}]\lambda\lambda 5007$ ). More recently, Qiu et al. (2024) constructed a sample of 304 galaxies with double-peaked  $\text{H}\alpha$ - $[\text{N II}]\lambda\lambda 6548,6583$  emission lines in MaNGA, each galaxy containing at least 5 spaxels requiring double Gaussian fitting. They found that these spaxels with double-peaked emission line structures are statistically associated with bars, AGNs, or tidal features. However, previous sample-based studies have not separated the two components of double-peaked emission line profiles and have not analyzed the physical properties of each component in detail.

In this work, we select 36 double-peaked narrow emission-line galaxies (DPGs) from the final data release of MaNGA survey and investigate the origin of their double-peaked emission line profiles by performing spatially resolved analyses on the kinematic properties and ionization mechanisms of each component. Different from Qiu

et al. (2024), we not only require sufficiently strong double-peaked  $\text{H}\alpha$ - $[\text{N II}]\lambda\lambda 6548,6583$  emission lines in the spectra, but also require that  $\text{H}\beta$ ,  $[\text{O III}]\lambda\lambda 4959,5007$ , and  $[\text{S II}]\lambda\lambda 6717,6731$  be sufficiently strong and exhibit double-peaked profiles, as these emission lines are necessary for BPT diagnostic diagrams. Additionally, we exclude ongoing mergers and galaxies with a narrow core component plus a broad wing component in the sample selection, which results in a smaller sample size. The paper is organized as follows. In Section 2, we give a brief introduction on the MaNGA survey and a detailed description of the sample selection method. In Section 3, we analyze the gas kinematics and the ionization mechanisms of the galaxies in our double-peaked sample. We discuss the possible origins of the double-peaked emission line profiles in DPGs in Section 4. Finally, we present our conclusions in Section 5. We adopt a flat  $\Lambda\text{CDM}$  cosmology with parameters  $H_0 = 70 \text{ km s}^{-1} \text{ Mpc}^{-1}$ ,  $\Omega_m = 0.3$ , and  $\Omega_\Lambda = 0.7$  throughout this paper.

## 2 DATA ANALYSIS

### 2.1 The MaNGA survey

MaNGA is one of the three core programs in the fourth-generation Sloan Digital Sky Survey (SDSS-IV; Blanton et al. 2017), using the 2.5 m Sloan Foundation Telescope at the Apache Point Observatory (Gunn et al. 2006). MaNGA employs dithered observations with 17 hexagonal IFUs (Law et al. 2015) with 5 sizes varying between 19 and 127 fibers (or 12.5–32.5 arcsec diameter in the sky) to explore the detailed internal structure of nearby galaxies (Drory et al. 2015). Two dual-channel BOSS spectrographs (Smee et al. 2013) provide simultaneous spectral coverage over 3,600–10,300 Å with a median spectral resolution of  $R \sim 2000$  (Law et al. 2016). The MaNGA project has conducted IFU observations of  $\sim 10,000$  nearby galaxies with a flat stellar mass distribution in  $9 \leq \log (M_*/M_\odot) \leq 11$  and a redshift coverage of  $0.01 < z < 0.15$  (Wake et al. 2017; Abdurro'uf et al. 2022).

The MaNGA Data Reduction Pipeline (DRP; Law et al. 2016) provides sky-subtracted and spectrophotometrically-calibrated 3D spectra for each individual galaxy. In addition, the MaNGA Data Analysis Pipeline (DAP; Westfall et al. 2019) analyzes datacube produced by the DRP and provides higher-level data products. The MaNGA DAP heavily uses pPXF (Cappellari & Emsellem 2004) and a selected subset of stellar templates from the MaStar library (Yan et al. 2019) to fit the stellar continuum, calculate absorption-line indices, and measure 21 prominent nebular emission lines in the MaNGA wavelength coverage. In this work, we use the MaNGA sample and DAP products drawn from SDSS DR17 (Abdurro'uf et al. 2022), which includes 10,010 unique galaxies. The MaNGA DAP products named "SPX-MILESCH-MASTARSSP" provide spatially resolved spectral properties, including stellar kinematics, properties of emission lines (e.g. fluxes, velocities, velocity dispersions, and equivalent widths), and spectral indices such as the 4000 Å break ( $D_n4000$ ). We also measure the global  $D_n4000$  for each galaxy from the stacked spectrum. We stack the spectra with median signal-to-noise ratio (S/N) per spaxel greater than 2 within the MaNGA bundle. Additionally, the redshift ( $z$ ), global stellar mass ( $M_*$ ), and effective radius ( $R_e$ , half-light radius in the  $r$ -band) are adopted from the NASA Sloan Atlas (NSA) catalog (Blanton et al. 2011), the Sérsic index  $n$  is adopted from MaNGA PyMorph photometric catalogue (Fischer et al. 2019).

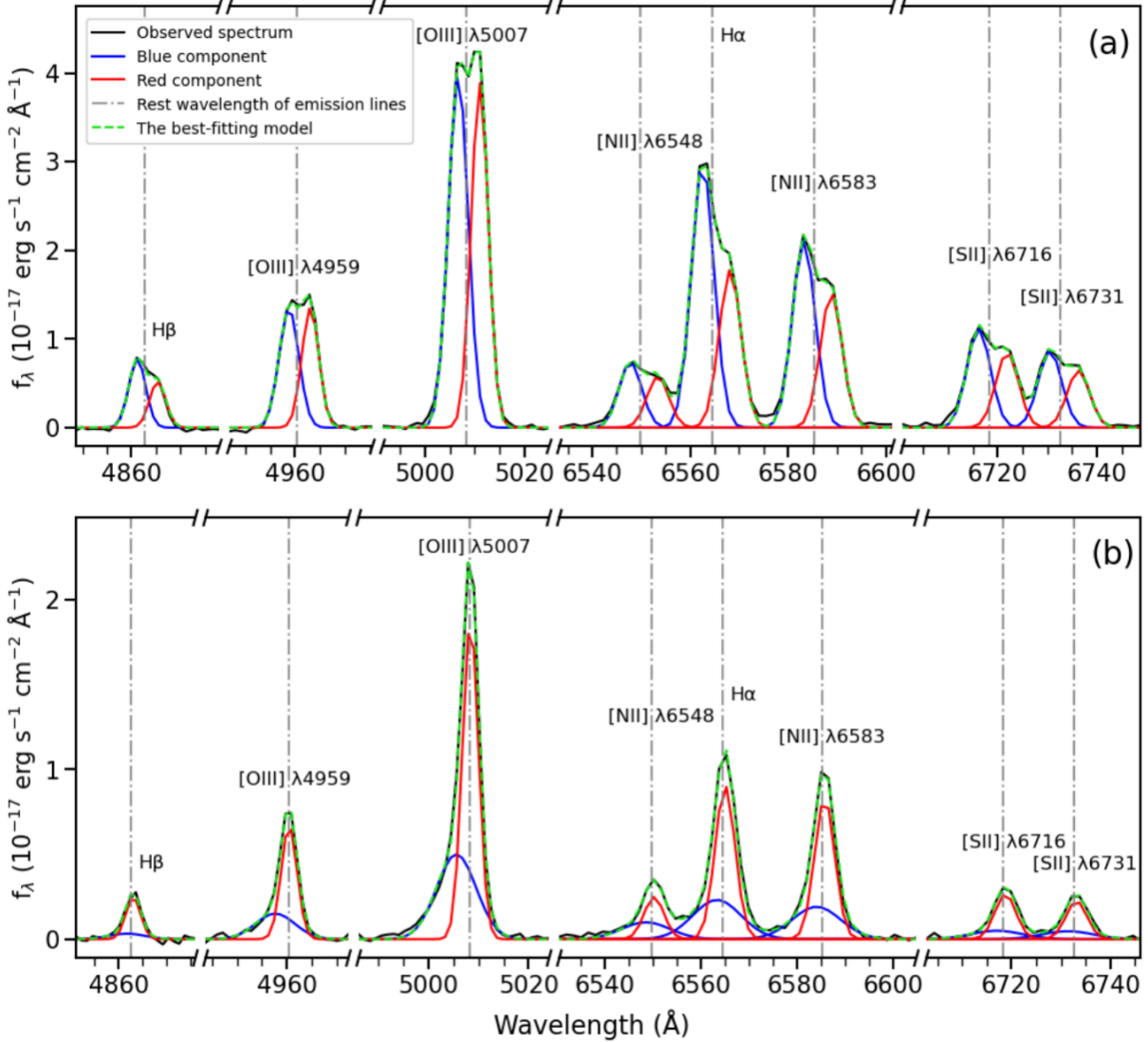


**Figure 1.** The emission line spectra from the central spaxel of two example galaxies. Panel (a): The spectrum of a double-peaked narrow emission-line galaxy (DPG, MaNGA ID: 1-339094). Panel (b): The spectrum of a galaxy exhibiting a narrow core and a broad wing in each emission line (MaNGA ID: 1-54940). In both panel, The black solid lines show the observed emission line spectra, while the blue and red solid lines represent the blue and red components of the double Gaussian model, respectively. The green dashed line represents the best-fit model, which is the combination of the blue and red components. In addition, the vertical gray dot-dashed lines mark the rest-frame wavelength centre of each emission line.

## 2.2 Sample selection

To ensure that the emissions of the  $[\text{O III}]\lambda 5007$  and  $\text{H}\alpha$  are sufficiently strong, we first select 1,837 out of 10010 galaxies in which the equivalent widths of both the  $[\text{O III}]\lambda 5007$  ( $\text{EW}_{[\text{O III}]}$ ) and  $\text{H}\alpha$  ( $\text{EW}_{\text{H}\alpha}$ ) in the central spaxel are greater than  $3 \text{ \AA}$ . We exclude 94 galaxies which show broad  $\text{H}\alpha$  emission lines in the central spaxel ( $\text{FWHM} > 1000 \text{ km s}^{-1}$ ).

For the remaining 1743 galaxies, we apply both the single and double Gaussian models to fit each emission line for spaxels with both  $\text{H}\alpha$  and  $[\text{O III}]\lambda 5007$   $\text{S/N} > 3$ .

### 2.2.1 Single Gaussian model

The single Gaussian model is constructed and implemented using the `curve_fit` function from the `scipy.optimize` module in Python

([Virtanen et al. 2020](#)). In the fitting process,  $\text{H}\beta$ ,  $[\text{N II}]\lambda\lambda 6548, 6583$ , and  $[\text{S II}]\lambda\lambda 6717, 6731$  emission lines are tied to have the same line centre and line width as  $\text{H}\alpha$  in the velocity space. We fit the  $[\text{O III}]\lambda\lambda 4959, 5007$  independently since their profiles do not typically match the profile of the other emission lines ([Reines et al. 2013](#)). Therefore, the  $[\text{O III}]\lambda 4959$  is tied to have the same line centre and line width as  $[\text{O III}]\lambda 5007$  in the velocity space.

The fitting of  $\text{H}\alpha$ ,  $[\text{N II}]\lambda\lambda 6548, 6583$ , and  $[\text{S II}]\lambda\lambda 6717, 6731$  emission lines is performed in the rest-frame wavelength range  $6520 \text{ \AA} \leq \lambda \leq 6760 \text{ \AA}$ , while the fitting of  $[\text{O III}]\lambda\lambda 4959, 5007$  is performed in the rest-frame wavelength range  $4930 \text{ \AA} \leq \lambda \leq 5030 \text{ \AA}$ . Additionally, the  $\text{H}\beta$  emission line is fitted in the range  $4840 \text{ \AA} \leq \lambda \leq 4890 \text{ \AA}$ . To ensure the fitting is effective for the narrow emission lines, we require the full width at half-maximum (FWHM) of each emission line to be less than  $1000 \text{ km s}^{-1}$ .

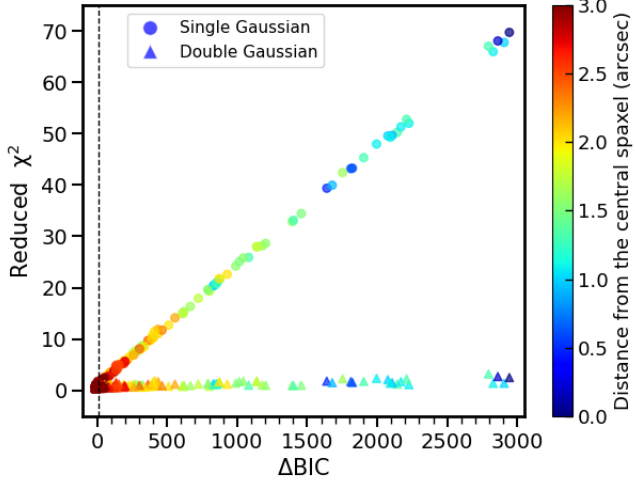


**Figure 2.** The relation between the  $\Delta\text{BIC}$  and reduced  $\chi^2$  for single and double Gaussian fittings of  $[\text{O III}]\lambda\lambda 4959, 5007$  region ( $4930\text{\AA} \leq \lambda \leq 5030\text{\AA}$ ) for a DPG example (MaNGA ID: 1-339094). For the circles, the Y-axis is calculated from the single Gaussian model, while the triangles represent the double Gaussian model. The data points are colour-coded by the distance to the galaxy centre. The vertical black dashed line marks the position where  $\Delta\text{BIC} = 10$ , above which the double Gaussian model provides a significantly better fitting than the single Gaussian model.

### 2.2.2 Double Gaussian model

For the double Gaussian fitting, we closely follow the method described in Section 2.2.1, the only difference is that each emission line is modeled by two Gaussian components.

We separate the two Gaussian components of each emission line into blue and red components. For each emission line, the line centre wavelength of the red component is required to be longer than that of the blue component ( $\lambda_{\text{blue}} < \lambda_{\text{red}}$ ). Fig. 1(a) shows the spectrum from the central spaxel of a DPG. The black solid line in Fig. 1 shows the observed emission line spectrum, while the blue and red solid lines represent the blue and red components of the double Gaussian model, respectively. The green dashed line represents the best-fit model, which is the combination of the blue and red components.

### 2.2.3 Bayesian Information Criterion

To determine which galaxies require double Gaussian models for emission line fitting, we use the Bayesian Information Criterion (BIC; Schwarz 1978; Liddle 2007) for both the single ( $\text{BIC}_{\text{single}}$ ) and double Gaussian models ( $\text{BIC}_{\text{double}}$ ). The definition of the BIC is:

$$\text{BIC} = \chi^2 + k \ln N, \quad (1)$$

where  $N$  is the number of data points,  $k$  is the number of free parameters in the model, and  $\chi^2$  is the chi-square of each model fitting. For each spaxel, we define  $\Delta\text{BIC}$  as:

$$\Delta\text{BIC} = \text{BIC}_{\text{single}} - \text{BIC}_{\text{double}}. \quad (2)$$

According to Swinbank et al. (2019) and Avery et al. (2021),  $\Delta\text{BIC} > 10$  indicates the single Gaussian model is insufficient for accurately describing the emission line profiles, whereas the double Gaussian model provides a significantly better fitting.

Fig. 2 shows the relation between the  $\Delta\text{BIC}$  and reduced  $\chi^2$  for single and double Gaussian fittings of  $[\text{O III}]\lambda\lambda 4959, 5007$  region

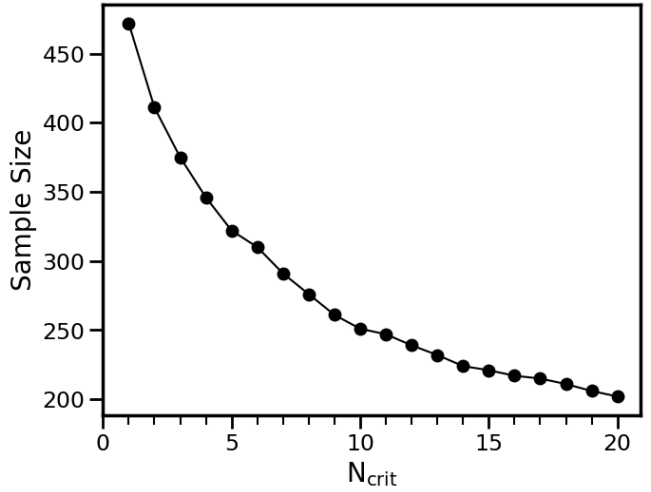


**Figure 3.** The sample size of double-peaked candidates as a function of the number of contiguous spaxels ( $N_{\text{crit}}$ ) that required to satisfying the two criteria of sample selection.

for a DPG. We calculate the reduced  $\chi^2$  of the single and double Gaussian models respectively. The circles represent the single Gaussian fittings, and the triangles represent the double Gaussian fittings, colour-coded by the distance to the galaxy centre. The vertical black dashed line marks the position where  $\Delta\text{BIC} = 10$ , above which the double Gaussian model provides a significantly better fitting than the single Gaussian model. We find that the difference in reduced  $\chi^2$  between the two models, as well as  $\Delta\text{BIC}$ , increases with decreasing distance to the galaxy centre. This suggests that the double Gaussian model is more necessary for the central regions than for the outskirts.

### 2.2.4 Selection of the DPG sample

For the 1,743 galaxies, we measure  $\Delta\text{BIC}$  for spaxels with both  $\text{H}\alpha$  and  $[\text{O III}]\lambda 5007$  emission lines  $\text{S/N} > 3$ . In order to be classified as a double-peaked candidate, a galaxy is required to have more than 10 contiguous spaxels satisfying the following criteria:

(i)  $\Delta\text{BIC} > 10$  for both the  $[\text{O III}]\lambda\lambda 4959, 5007$  region and the  $\text{H}\alpha$  region. Namely, each emission line should be modelled by a double Gaussian model.

(ii) The flux ratio between the blue and red components is in the range of  $[0.1, 10]$  for both the  $[\text{O III}]\lambda\lambda 4959, 5007$  and  $\text{H}\alpha$  regions (Wang et al. 2009). This flux ratio limit can effectively exclude the influence of the background noise.

Based on these criteria, 225 galaxies are selected as double-peaked candidates. In fact, the number of double-peaked candidates selected by this method changes with the number of contiguous spaxels ( $N_{\text{crit}}$ ) that required to satisfying the above two criteria. Fig. 3 shows the sample size as a function of  $N_{\text{crit}}$ .

It is clear that the sample size decreases quickly from 472 at  $N_{\text{crit}} = 1$  to 225 at  $N_{\text{crit}} = 15$ . The downward trend slows down at  $N_{\text{crit}} > 15$ . Considering that the typical MaNGA point spread function (PSF) is modeled as a circular Gaussian with  $\text{FWHM} \sim 2.5$  arcsec (5 spaxels; Law et al. 2015). In this work, we use  $N_{\text{crit}} = 15$  for the sample selection, corresponding to about three times the MaNGA PSF FWHM, to ensure that the detected features are spatially resolved.

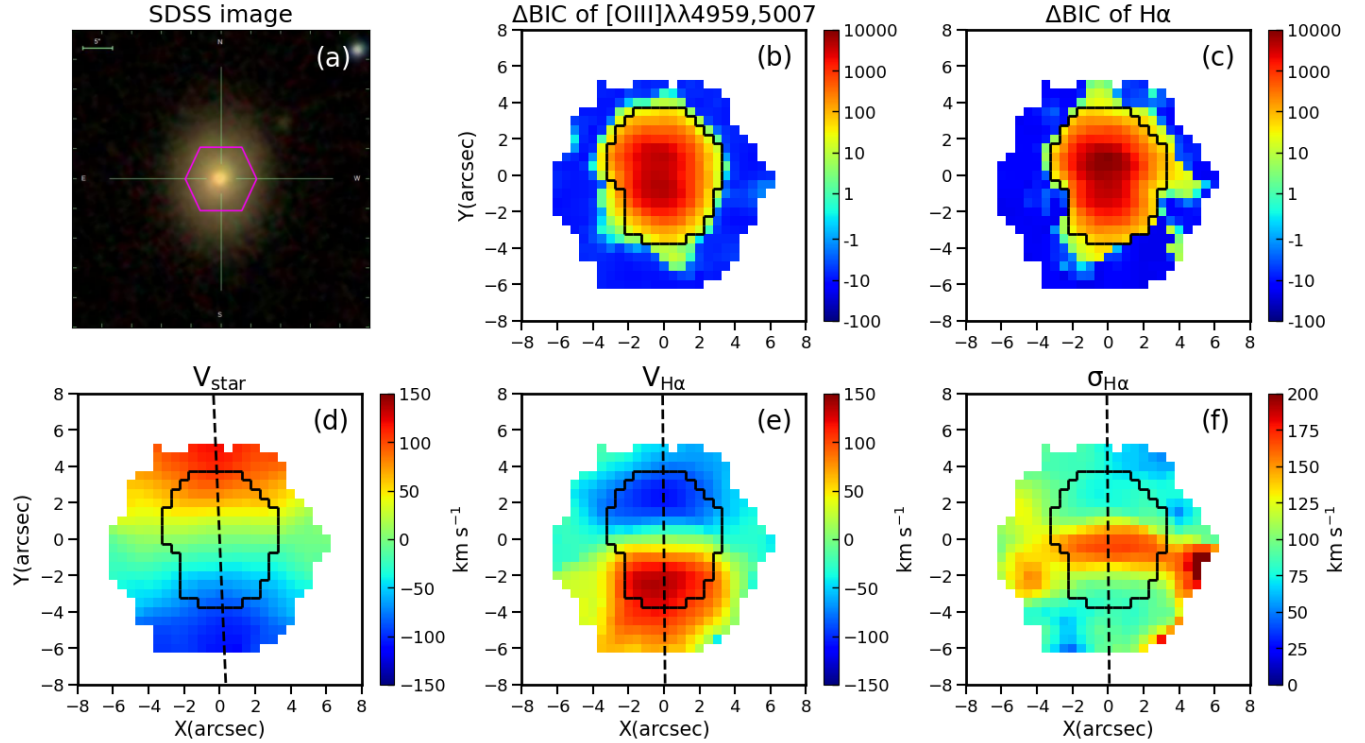


**Figure 4.** The spatial distributions of  $\Delta\text{BIC}$ , stellar velocity,  $\text{H}\alpha$  velocity and  $\text{H}\alpha$  velocity dispersion of a DPG example (MaNGA ID: 1-339094). Panel (a): The SDSS  $g$ -,  $r$ -,  $i$ -band image. Panel (b) & (c): The  $\Delta\text{BIC}$  maps for  $[\text{O III}]\lambda\lambda4959,5007$  and  $\text{H}\alpha$  regions, respectively. Panel (d): The stellar velocity field, the black dashed line represent the kinematic major axis of the stellar component. Red represents moving away from us while blue represents moving toward us. Panel (e) & (f): The velocity field and the velocity dispersion field of  $\text{H}\alpha$ , the black dashed line represent the kinematic major axis of the gaseous component. Spaxels within the black polygons in panel (b) ~ (f) have  $\Delta\text{BIC} > 10$  for both the  $[\text{O III}]\lambda\lambda4959,5007$  and  $\text{H}\alpha$  regions.

We visually inspect these 225 double-peaked candidates and classify them into two categories:

(i) 53 galaxies exhibit double-peaked narrow profiles in  $[\text{O III}]\lambda5007$ ,  $\text{H}\alpha$ , as well as other emission lines ( $\text{H}\beta$ ,  $[\text{O III}]\lambda4959$ ,  $[\text{N II}]\lambda\lambda6548,6583$ , and  $[\text{S II}]\lambda\lambda6717,6731$ ), as shown in Fig. 1(a). The two components of the double-peaked emission line profiles have similar velocity dispersions ( $0.67 < \sigma_{\text{blue}}/\sigma_{\text{red}} < 1.5$ ), where  $\sigma_{\text{blue}}$  and  $\sigma_{\text{red}}$  represent the velocity dispersions of the blue and red components, respectively.

(ii) 172 galaxies show a narrow core and a broad wing component, as shown in Fig. 1(b). The velocity dispersion of the broad wing component is 1.5 times larger than the narrow core component ( $\sigma_{\text{broad}}/\sigma_{\text{narrow}} > 1.5$ ). The broad wing components in these galaxies are suggested as outflow contribution (Greene & Ho 2005; Woo et al. 2016; Karouzos et al. 2016).

In this work, we do not include the outflow candidates in our double-peaked sample. For the remaining 53 galaxies exhibiting double-peaked emission line profiles, we visually exclude 17 ongoing mergers, in which the two narrow emission components may be primarily contributed by the gas of the two galaxies in merging, leaving 36 DPGs as our final sample. Other external effects that could generate double-peaked line profiles are discussed in Section 4.4.

Fig. 4 shows the spatially resolved  $\Delta\text{BIC}$  and the kinematics of a DPG example (MaNGA ID: 1-339094). Fig. 4(a) shows the SDSS  $g$ -,  $r$ -,  $i$ -band image. Fig. 4(b) & (c) show the  $\Delta\text{BIC}$  maps for  $[\text{O III}]\lambda\lambda4959,5007$  and  $\text{H}\alpha$  regions for spaxels where both the  $\text{H}\alpha$  and  $[\text{O III}]\lambda5007$  S/N > 3. Spaxels within the black polygon in Fig. 4 have  $\Delta\text{BIC} > 10$  for both the  $[\text{O III}]\lambda\lambda4959,5007$  and  $\text{H}\alpha$  regions.

Fig. 4(d), (e) and (f) show the stellar velocity field, the  $\text{H}\alpha$  velocity and velocity dispersion fields provided by MaNGA DAP with single Gaussian fitting of each emission line, respectively. In the velocity fields, red represents moving away from us while blue represents moving toward us. The black dashed lines represent the kinematic major axes of the stellar (Fig. 4d) and gaseous (Fig. 4e & f) components fitted by the `fit_kinematic_pa` module in Python (Krajnović et al. 2006).

As shown in Fig. 4(d) & (e), the stellar and gaseous discs are counter-rotating. As Fig. 4(f) shows, the  $\text{H}\alpha$  velocity dispersion field exhibits an enhanced region along the minor axis. In this region, the blue and red components have similar fluxes and show an obvious double-peaked profile. The single Gaussian fitting represents the combined contribution of the two components, resulting in a higher velocity dispersion.

### 2.3 Control sample

In order to understand the origin of the double-peak profiles, we build a control sample for comparison. The control sample is selected from the galaxies with both the  $\text{EW}_{[\text{O III}]}$  and  $\text{EW}_{\text{H}\alpha} > 3 \text{ \AA}$  for the central spaxel. For each DPG, we select a control galaxy (CG) whose emission line shows single Gaussian structure. The criteria for selecting the control sample are summarized below:

(i) We stack the spectra of spaxels within a circular aperture of central 1 kpc radius for each galaxy, following the method of Albán & Wylezalek (2023). The emission line ratios measured from the stacked spectra are required to fall within the same ionization region

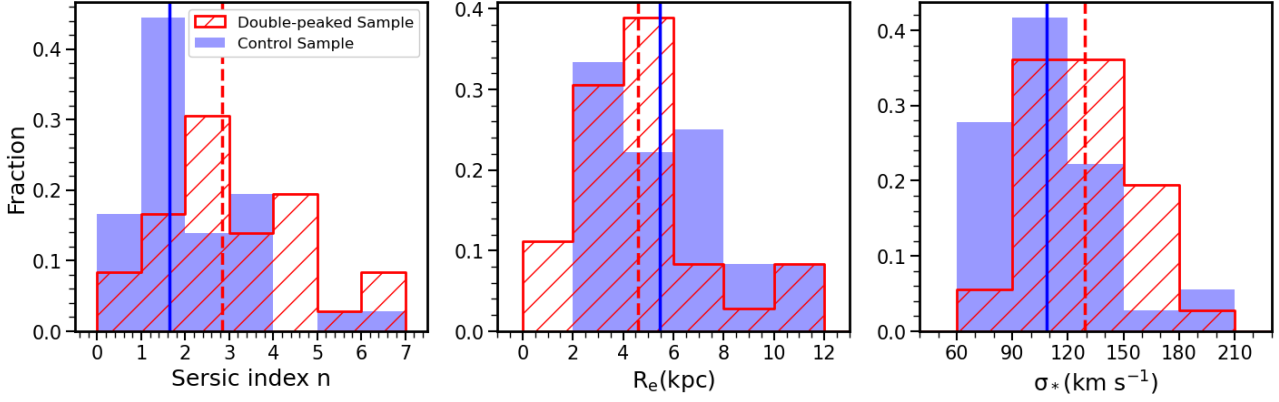


**Figure 5.** Distributions of the Sérsic index ( $n$ , left), effective radius ( $R_e$ , middle) and stellar velocity dispersion ( $\sigma_*$ , right) for the double-peaked sample (red) and the control sample (blue). The vertical red dashed and blue solid lines mark the median values of each distribution for the double-peaked sample and the control sample, respectively.

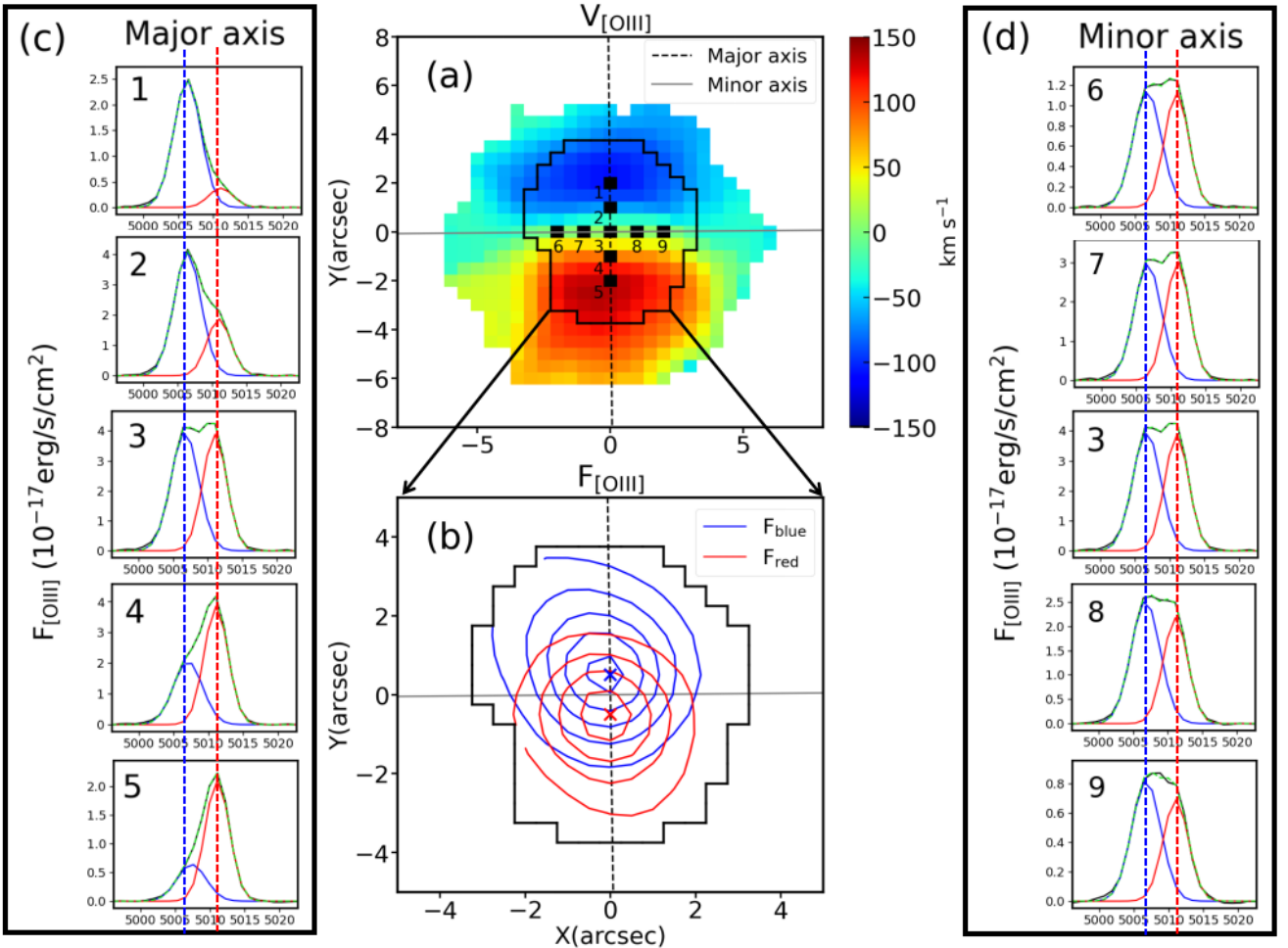


**Figure 6.** Panel (a): The  $[\text{O III}]\lambda 5007$  velocity field of MaNGA 1-339094 provided by the MaNGA DAP based on a single-Gaussian fit. Spaxels within the black polygon require double Gaussian fitting. The black dashed line represents the kinematic major axis of the gaseous component, while the grey solid line marks the kinematic minor axis. The black squares mark the spaxels whose spectra are shown in panel (c) & (d). Panel (b): The  $[\text{O III}]\lambda 5007$  flux contours of the blue and red components for spaxels requiring double Gaussian fitting. The blue and red crosses mark the positions of peak fluxes of the blue and red components, respectively. Panel (c) & (d): The  $[\text{O III}]\lambda 5007$  emission line spectra for five spaxels along the major axis (1, 2, 3, 4, 5) and five spaxels along the minor axis (6, 7, 3, 8, 9). The black solid spectra are the observed emission lines, while the blue and red solid curves represent the blue and red Gaussian components, respectively. The green dashed line shows the best-fit model, which is the combination of the blue and red components. The vertical blue and red dashed lines mark the  $[\text{O III}]\lambda 5007$  line centres of the blue and red components for the central spaxel, spaxel 3.

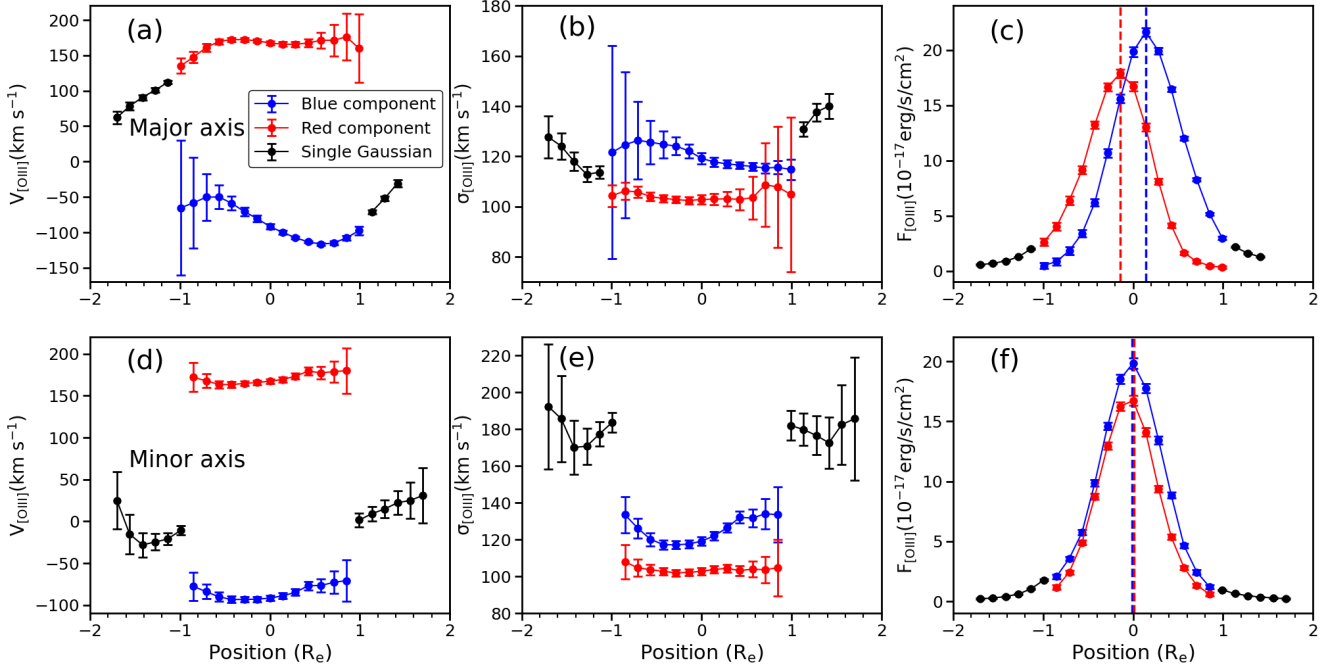


**Figure 7.** The velocity (left), velocity dispersion (middle), and flux (right) for the blue and red components of the  $[\text{O III}]\lambda 5007$  emission line along the major (top row) and minor (bottom row) axes for MaNGA 1-339094. The blue and red dots represent the blue and red components, respectively. The black dots are the single Gaussian fitting results for spaxels with  $\Delta\text{BIC} < 10$ . The error bars show the  $\pm 1\sigma$  scattering ranges. The vertical blue and red dashed lines in panel (c) & (f) mark the positions of the peak fluxes of the blue and red components, respectively.

in the  $[\text{S II}]\text{-BPT}$  diagram (Baldwin et al. 1981; Kewley et al. 2001) as that of the DPGs based on single Gaussian fitting. This criterion ensures that the central regions of both the DPGs and their CGs are ionized by the same mechanism.

(ii)  $|\Delta \log M_*| \leq 0.1$ . For each DPG, we constrain the corresponding CG to have a similar stellar mass. Stellar mass is the most fundamental parameter of a galaxy and is closely associated with many other physical parameters.

(iii)  $|\Delta D_n 4000| \leq 0.05$ . The CGs and DPGs are constrained to have similar global  $D_n 4000$  to ensure that they have similar stellar populations.

Fig. 5 shows the distributions of the Sérsic index ( $n$ ), effective radius ( $R_e$ ) and the flux-weighted mean stellar velocity dispersion ( $\sigma_*$ ) within  $1 R_e$ , for the double-peaked sample (red) and the control sample (blue). The stellar velocity dispersion is measured by MaNGA DAP. The vertical red dashed and blue solid lines mark the median values of the each distribution for the double-peaked sample and the control sample. As shown in the left panel of Fig. 5, the median value of Sérsic index  $n$  in our double-peaked sample is  $n \sim 3$ , while the median value for the control sample is  $n \sim 1.5$ . The larger Sérsic index  $n$  of double-peaked sample indicating that the DPGs may have larger bulges than CGs. The middle panel of Fig. 5 shows that the median value of  $R_e$  in our double-peaked sample is  $\sim 1$  kpc smaller than the control sample. The right panel of Fig. 5 shows that the median value of  $\sigma_*$  is  $\sim 20 \text{ km s}^{-1}$  larger than the control sample.

## 3 RESULTS

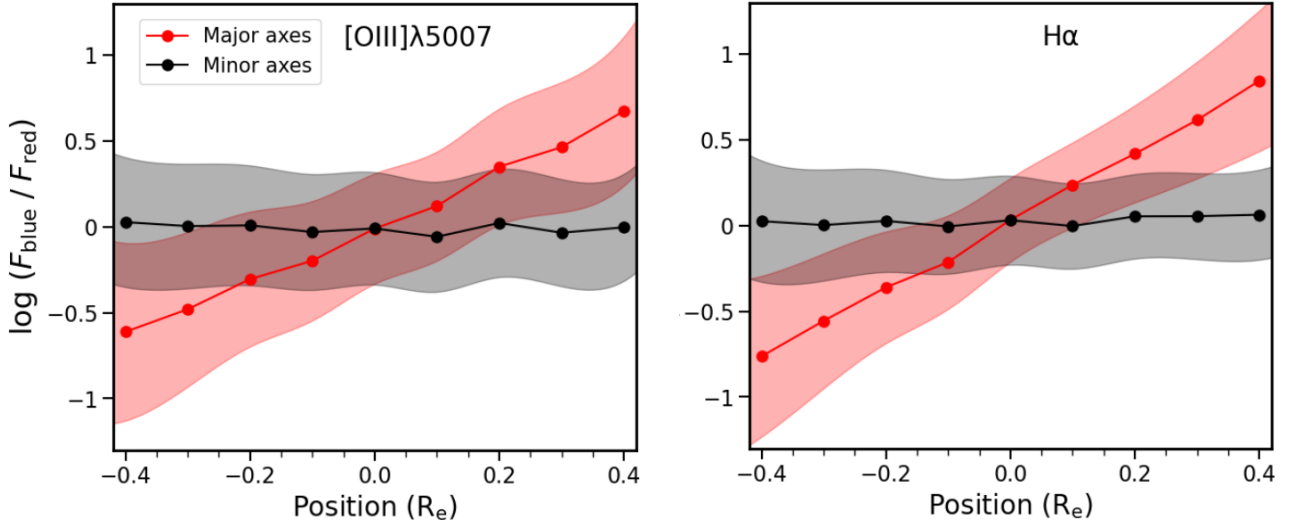
### 3.1 Gas kinematics

In this section, we calculate the spatially resolved kinematic parameters and fluxes for the blue and red components of both  $[\text{O III}]\lambda 5007$

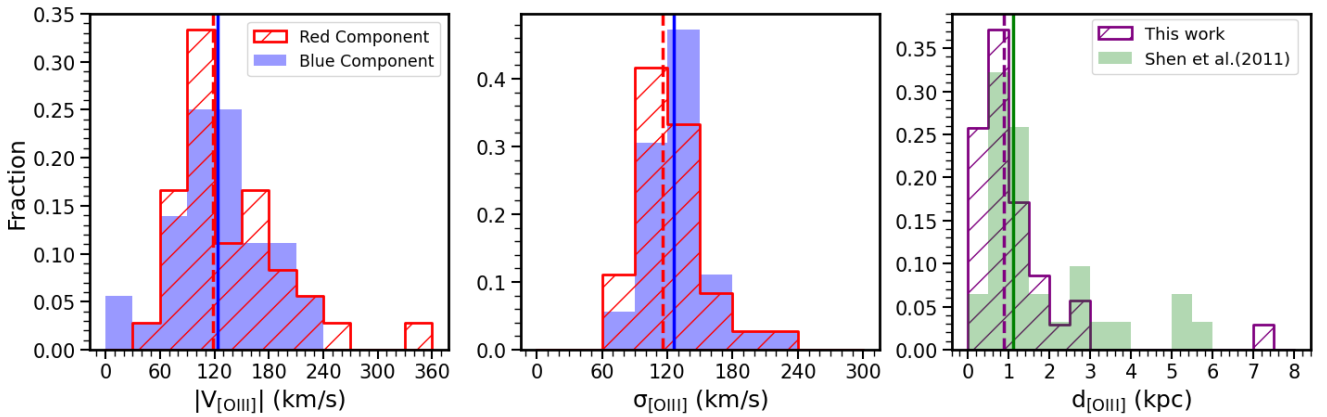
and  $\text{H}\alpha$  through the double Gaussian fitting. Although we have not tied the line centre and line width in the fitting process, the main results derived from  $\text{H}\alpha$  are consistent with those from  $[\text{O III}]\lambda 5007$ . Here we only present the results of  $[\text{O III}]\lambda 5007$  fitting as an example.

Fig. 6 shows the result of MaNGA 1-339094 as an example. Fig. 6(a) shows the  $[\text{O III}]\lambda 5007$  velocity field provided by the MaNGA DAP based on a single-Gaussian fit. Spaxels within the black polygon require double Gaussian fitting. The black dashed line represents the kinematic major axis of the gaseous component, while the grey solid line marks the kinematic minor axis. The black squares mark the spaxels whose spectra are shown in Fig. 6(c) & (d). The blue and red contours in Fig. 6(b) show the  $[\text{O III}]\lambda 5007$  flux distributions of the blue ( $F_{\text{blue}}$ ) and red ( $F_{\text{red}}$ ) components for spaxels requiring double Gaussian fitting, respectively. The blue and red crosses mark the positions of peak fluxes of the blue and red components. The black dashed and grey solid lines are same as Fig. 6(a). Fig. 6(c) shows the  $[\text{O III}]\lambda 5007$  emission line spectra for five spaxels along the major axis (1, 2, 3, 4, 5), while Fig. 6(d) shows the spectra for five spaxels along the minor axis (6, 7, 3, 8, 9). In each spectrum of Fig. 6(c) & (d), the black solid line represents the observed emission line spectrum, the blue and red solid lines represent the blue and red components, respectively. The green dashed line shows the best-fit model, which is the combination of the blue and red components. The vertical blue and red dashed lines mark the  $[\text{O III}]\lambda 5007$  line centres of the blue and red components for the central spaxel, spaxel 3. As shown in Fig. 6(c) & (d), the line centres of both the blue and red components exhibit no significant variations across different spatial positions.

Fig. 7 shows the velocity (left), velocity dispersion (middle), and flux (right) for the blue and red components of the  $[\text{O III}]\lambda 5007$  emission line along the major (top row) and minor (bottom row) axes for MaNGA 1-339094. The blue and red dots represent the blue and red components, respectively. The black dots are the single Gaussian fitting results for spaxels with  $\Delta\text{BIC} < 10$ . The error bars show the  $\pm 1\sigma$  scattering ranges. The vertical blue and red dashed lines in panel (c) & (f) mark the positions of the peak fluxes of the blue and red components, respectively.



**Figure 8.** The  $[\text{O III}]\lambda 5007$  (left) and  $\text{H}\alpha$  (right) flux ratios between the blue and red components along the major and minor axes in DPGs. For each panel, the red and black dots represent the median of the flux ratios along the major and minor axes for 35 DPGs, respectively. The position on the X-axis is positive on the blueshifted side of the  $[\text{O III}]\lambda 5007$  velocity field and negative on the redshifted side. The shadow regions show the  $\pm 1\sigma$  scattering ranges.



**Figure 9.** The distributions of the line-of-sight velocities (left) and velocity dispersions (middle) for  $[\text{O III}]\lambda 5007$ . The blue (red) component is shown in blue (red) histogram. The right panel compares the separation distance of the peak fluxes for the blue and red  $[\text{O III}]\lambda 5007$  components in our work (purple) and that (green) in [Shen et al. \(2011\)](#). The median value of each distribution is marked by the vertical line with the same colour as the distribution.

red components, respectively. The black dots are the single Gaussian fitting results for spaxels with  $\Delta\text{BIC} < 10$ . The error bars show the  $\pm 1\sigma$  scattering ranges. The vertical blue and red dashed lines in Fig. 7(c) & (f) mark the positions of the peak fluxes of the blue and red components, respectively.

Both Fig. 6 and Fig. 7(c) & (f) show that along the major axis, significant variations can be observed in the line profile and in the flux ratio between the blue and red components; whereas along the minor axis, there is no obvious variation in either the flux ratio or the line profile.

As shown in Fig. 6(c) & (d) and Fig. 7(a) & (d), both the blue and red components exhibit no obvious velocity variations along the major or minor axes. For MaNGA 1-339094, the blue (red) component exhibits a velocity of  $\sim -90 \text{ km s}^{-1}$  ( $\sim 160 \text{ km s}^{-1}$ ), relative to the stellar velocity of the central spaxel. In addition, Fig. 7(b) & (e) show that the velocity dispersions of both the blue and red components keep roughly a constant along either the major or minor axes.

The blue component exhibits a velocity dispersion of  $\sim 120 \text{ km s}^{-1}$ , while the red component has a velocity dispersion of  $\sim 100 \text{ km s}^{-1}$ .

Additionally, Fig. 7(a) & (c) show that along the major axis, the velocity and flux of the single Gaussian fitting in the outskirts (black dots) are the natural continuation of one of the double Gaussian components for the inner region. In contrast, Fig. 7(d) & (f) show that along the minor axis, the velocity and flux of the single Gaussian component in the outskirts are not consistent with either the blue or the red component for the inner region. Combining Fig. 7(b) & (e), we find that the velocity dispersion of the single Gaussian fitting along the minor axis is larger than that along the major axis, consistent with the result of enhanced velocity dispersion along the minor axis in Fig. 4(f).

From Fig. 6(b), we find that the flux distributions of the blue and red components deviate from each other along the major axis. The vertical blue and red dashed lines in Fig. 7(c) & (f) show that along the major axis, the peak fluxes of the blue and red components have a separation of  $\sim 0.3 R_e$ , which corresponds to  $\sim 0.65 \text{ kpc}$ ; whereas

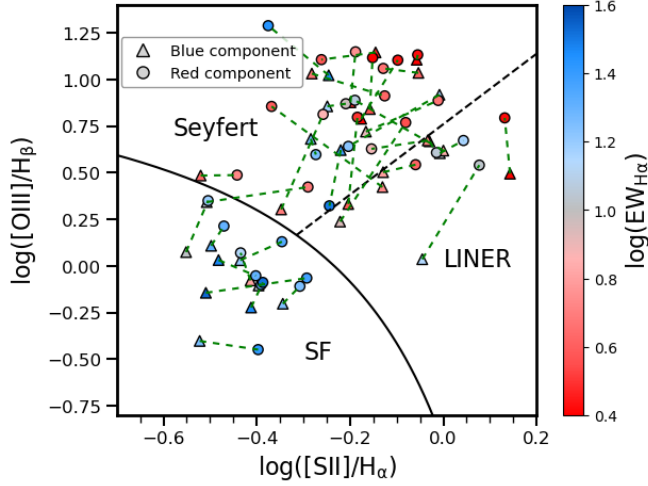


**Figure 10.** The [S II]-BPT diagram for the blue (triangles) and red (circles) components measured from the stacked spectra of the central 1 kpc circular region. The data points are colour-coded by the equivalent width of  $H\alpha$  ( $EW_{H\alpha}$ ). The black solid curve (Kewley et al. 2001) represents the demarcation line that separates AGN and star-forming (SF) galaxies/regions. The black dashed straight line (Kewley et al. 2006) distinguishes Seyferts from LINERs. In addition, the dashed green lines connect the two components of the same galaxy.

along the minor axis, the positions of the peak fluxes of the two components overlap with each other. In addition, Fig. 7(f) shows that the two components have comparable fluxes along the minor axis, leading to the enhanced velocity dispersion observed in the single Gaussian fitting shown in Fig. 7(e).

The analysis above focuses on the individual DPG. To further explore whether similar kinematic properties are statistically present in DPGs, we measure the  $[OIII]\lambda 5007$  and  $H\alpha$  flux ratios between the blue and red components along the major and minor axes for all 36 DPGs. We find that 35 out of these 36 DPGs show similar properties as MaNGA 1-339094. Fig. 8 shows the  $[OIII]\lambda 5007$  (left) and  $H\alpha$  (right) flux ratios between the two components along the major and minor axes for these 35 DPGs. In each panel, the red and black dots represent the median flux ratios along the major and minor axes, respectively. The position on the X-axis is positive on the blueshifted side of the  $[OIII]\lambda 5007$  velocity field and negative on the redshifted side. The shadow regions show the  $\pm 1\sigma$  scattering ranges. Both the median flux ratios between the two components of  $[OIII]\lambda 5007$  and  $H\alpha$  show a steep gradient along the major axes. In contrast, there are no obvious variations in the median flux ratios along the minor axes.

Fig. 9 shows the distributions of line-of-sight velocities (left) and velocity dispersions (middle) of the blue and red  $[OIII]\lambda 5007$  components. The median value of each distribution is marked with a vertical line of the same colour. It is clear that the median values of the line-of-sight velocities and the velocity dispersions for the red and blue components are similar. This similar kinematic properties of the two Gaussian components indicate that the two emission line clouds have the same origin. The right panel compares the separation distance ( $d_{[OIII]}$ ) of the peak fluxes for the blue and red  $[OIII]\lambda 5007$  components in our work (purple) and that (green) in Shen et al. (2011). The vertical purple dashed and green solid lines mark the median values of each distribution. Most DPGs in our sample have a spatial separation  $< 3$  kpc, with a median value of  $\sim 1$  kpc, consistent with that given in Shen et al. (2011).

### 3.2 Ionization mechanisms

Mapping diagnostic line ratios across a galaxy can give us insights into the ionization state of the gas. The widely used system for spectral classification of emission-line galaxies is based on the diagnostic diagrams originally suggested by Baldwin et al. (1981, generally referred to as BPT diagrams). Standard BPT diagnostic diagrams rely on the emission line ratios  $[OIII]\lambda 5007/H\beta$  versus  $[OI]\lambda 6300/H\alpha$ ,  $[SII]\lambda\lambda 6717,6731/H\alpha$  or  $[NII]\lambda 6583/H\alpha$  (Kewley et al. 2001). In both  $[OI]\lambda 6300$  and  $[SII]\lambda\lambda 6717,6731$  BPT diagrams, high ionization Seyfert regions/galaxies and low-ionization narrow emission-line regions (LINERs; Stasińska et al. 2008) have been shown to be located on two distinct sequences. In the current work, we choose to use the [S II]-BPT diagram since the S/N of  $[SII]\lambda\lambda 6717,6731$  is much higher than  $[OI]\lambda 6300$  in most spectra.

Fig. 10 shows the [S II]-BPT diagrams for the blue (triangles) and red (circles) components measured from the stacked spectra of the central 1 kpc circular region. The data points are colour-coded by the equivalent width of  $H\alpha$  ( $EW_{H\alpha}$ ; Sánchez 2020; Riffel et al. 2023). The dashed green lines connect the two components of the same galaxy. The black solid curve (Kewley et al. 2001) is the demarcation line that separates the AGN and star-forming (SF) galaxies/regions, and the black dashed straight line (Kewley et al. 2006) distinguishes Seyferts from LINERs.

As shown in Fig. 10, SF DPGs exhibit significantly larger  $EW_{H\alpha}$  than Seyfert/LINER DPGs. For 83.3% (30/36) DPGs, both the blue and red components are located in the same ionization region in the [S II]-BPT diagram and exhibit similar  $EW_{H\alpha}$ , which suggests that the two components are ionized by similar sources. Specifically, 41.7% (15/36) of the DPGs have both blue and red components classified as Seyfert, 13.9% (5/36) as LINER, and 27.7% (10/36) as SF. The remaining 16.7% (6/36) DPGs have their blue and red components located in different ionization regions. The main results keep the same if we use [N II]-BPT instead of the [S II]-BPT. The high fraction of AGN in the DPG sample could be due to a relatively high proportion of tidal interaction (Rembold et al. 2024; Raimundo et al. 2023) or because of a selection effect that we require high  $EW_{[OIII]}$  for sample selection.

## 4 THE ORIGIN OF DPGS

In this section, we discuss the possible origins of the double-peaked emission line profiles of our sample based on observational results listed in Section 3.

### 4.1 Dual AGNs

According to the definition of dual AGNs, both the blue and red components are required to be located in the Seyfert or LINER region of the BPT diagram (Wang et al. 2009). In the [S II]-BPT diagram, 41.7% of DPGs have both the blue and red components classified as Seyfert, and 13.9% are classified as LINER. LINERs were first proposed by Heckman (1980), and initially classified as low-luminosity AGNs. Recently, several studies based on IFU observations suggest that the physical size of the LINER regions can extend to kpc scales, and most galaxies with LINER regions are unlikely to be low-luminosity AGNs (Sarzi et al. 2010; Belfiore et al. 2016). This indicates that the origin of double-peaked emission line profiles is not necessarily associated with AGN activities.

Additionally, Blecha et al. (2013) suggested that with insufficient spatial resolution in photometric observations, a dual AGN system

separated by  $\sim$  kpc cannot be resolved, resulting in a measured photometric major axis of the host galaxy aligning with the orientation connecting the two AGNs. Nevin et al. (2016) simulated the long-slit observational features of a dual AGN model. They find that along the orientation connecting the two AGNs, the flux ratio between the two narrow emission line components shows systematic variations; while perpendicular to this orientation, the flux ratio shows almost no variation.

Although we find that the flux ratio between the blue and red components varies systematically along the major axes and keeps roughly a constant along the minor axes in 97.2% (35/36) DPGs (see Fig. 8), we do not suggest the double-peaked line profiles are dominated by dual AGNs. As known from the literatures, only a very small fraction ( $\sim 2\%$ ; Fu et al. 2012) of double-peaked AGNs are expected to be dual AGNs.

## 4.2 Rotating discs

If the double-peaked emission line profiles originate from a rotating disc, we would expect the flux ratio between the two components varies along the major axis, while this ratio keeps a constant along the minor axis (Shen et al. 2011; Müller-Sánchez et al. 2015; Nevin et al. 2016; Maschmann et al. 2023). In the central regions, the two components have comparable fluxes. Towards the outskirts along half major axis, one component gradually dominates the line profile, while the other weakens until it becomes undetectable. This expectation is totally consistent with the observational results shown in Fig. 6 and Fig. 8. Additionally, Fig. 7(a) & (c) show that along the major axis, the velocity and flux of the single Gaussian component in the outskirts are the natural continuation of the blue or red  $[\text{O III}]\lambda 5007$  component for the inner region.

Furthermore, the two components of the double-peaked profile resulting from rotating discs show similar value of line-of-sight velocities and similar velocity dispersions according to the axisymmetric models in Maschmann et al. (2023). As shown in Fig. 9, the blue and red components of our sample exhibit similar distributions in both the value of line-of-sight velocity and velocity dispersion. Thus, we suggest that the double-peaked emission line profiles in 35 out of 36 DPGs primarily originate from rotating discs.

In order to examine whether dynamic disturbances present in the rotating discs, we check the flux ratio between the blue ( $F_{\text{blue}}$ ) and red ( $F_{\text{red}}$ ) components of both  $\text{H}\alpha$  and  $[\text{O III}]$  emission lines for the central spaxel of each galaxy. 22.9% (8/35) DPGs have  $0.75 \leq F_{\text{blue}}/F_{\text{red}} \leq 1.25$  for both  $\text{H}\alpha$  and  $[\text{O III}]$  emission lines. We suggest undisturbed rotating discs as the origin of double-peaked emission line profiles in these galaxies. In contrast, 77.1% (27/35) DPGs have  $F_{\text{blue}}/F_{\text{red}} > 1.25$  or  $F_{\text{blue}}/F_{\text{red}} < 0.75$  in the central spaxel, these asymmetric line profiles might be due to dynamic disturbances in the rotating discs.

## 4.3 Outflows

Galactic-scale outflows are known to be powered by star formation or AGN activities. In actively star-forming galaxies, galactic-scale outflows are driven by the mechanical energy and momentum from supernovae and stellar winds (Heckman et al. 1990). Young star clusters create overpressured bubbles of hot gas that expand and sweep up surrounding interstellar medium (ISM) until they ‘blow out’ from the disc into the halo. The collective action of multiple superbubbles results in a weakly collimated biconical outflow along the minor axis of the galaxy (Chen et al. 2010; Sakamoto et al.

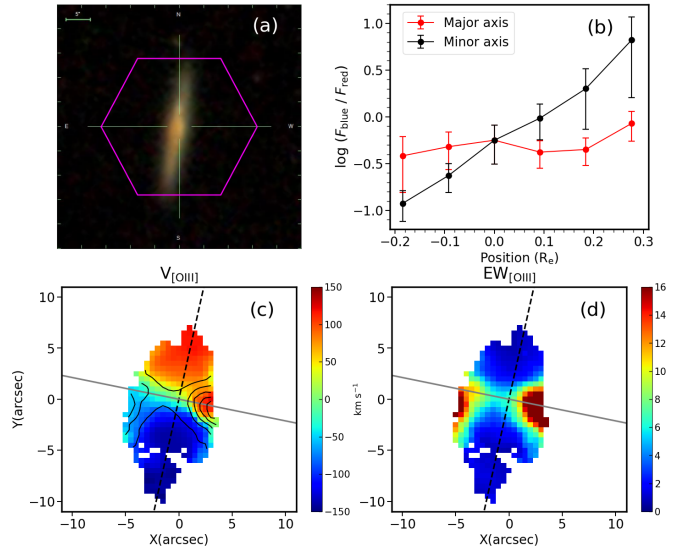


**Figure 11.** Panel (a): The SDSS  $g$ -,  $r$ -,  $i$ -band image of the DPG with biconical outflow (MaNGA ID: 1-210020). Panel (b): The  $[\text{O III}]\lambda 5007$  flux ratios between the blue and red components along the major (red) and minor axes (black). The error bars show the  $\pm 1\sigma$  scattering ranges. The position on the X-axis is positive on the blueshifted side of the  $[\text{O III}]\lambda 5007$  velocity field and negative on the redshifted side. Panel (c) & (d): The velocity map and the equivalent width map of  $[\text{O III}]\lambda 5007$ , the black dashed line represent the kinematic major axis of the gaseous component, while the grey solid line mark the minor axis. The black contours in panel (c) mark the regions with enhanced  $\text{EW}_{[\text{O III}]}$ .

2014). In AGN host galaxies, galactic-scale outflows are driven by wide-angle winds launched from the accretion disc, accelerated by thermal energy, radiation pressure, or radio jets (Fabian 2012; Russell et al. 2019; Veilleux et al. 2020).

Our results of Fig. 6 and Fig. 8 are inconsistent with the biconical outflow model, in which the flux ratio between the blue and red components is expected to vary significantly along the minor axis of the galaxy (Fischer et al. 2017). However, we identify one DPG (MaNGA ID: 1-210020) whose  $[\text{O III}]\lambda 5007$  flux ratio between the two Gaussian components shows significant variation along the minor axis, while it keeps roughly a constant along the major axis as shown in Fig. 11. Fig. 11 shows that this DPG is an edge-on galaxy with a biconical ionized structure in the  $\text{EW}_{[\text{O III}]}$  map along the minor axis. Fig. 11(a) shows the SDSS  $g$ -,  $r$ -,  $i$ -band image. Fig. 11(b) shows the  $[\text{O III}]\lambda 5007$  flux ratios between the blue and red components along the major (red) and minor axes (black). The error bars show the  $\pm 1\sigma$  scattering ranges. The position on the X-axis is positive on the blueshifted side of the  $[\text{O III}]\lambda 5007$  velocity field and negative on the redshifted side. Fig. 11(c) & (d) show the velocity map and the equivalent width map of  $[\text{O III}]\lambda 5007$ , the black dashed line represent the kinematic major axis of the gaseous component, while the grey solid line mark the minor axis. The black contours in panel (c) mark the regions with enhanced  $\text{EW}_{[\text{O III}]}$ . The velocity field within the two  $\text{EW}_{[\text{O III}]}$  enhanced regions clearly deviates from regular disk rotation due to outflow contribution (Bao et al. 2019, 2021; Zhou et al. 2024). Thus, we suggest that the origin of double-peaked profiles in this DPG is associated with biconical outflow.

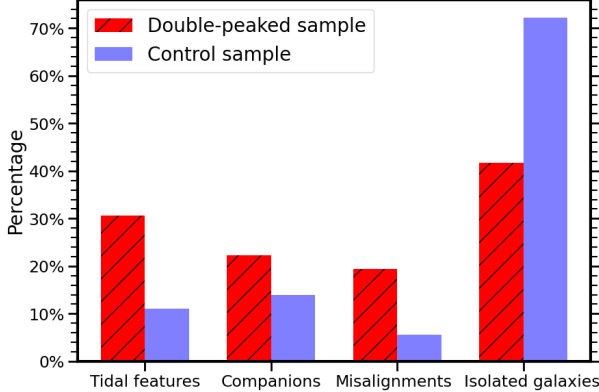


**Figure 12.** Classification of galaxies with different features for double-peaked sample (red histograms) and their control sample (blue histograms).

#### 4.4 External processes in DPGs

In 77.1% of DPGs in our sample, the emission lines show asymmetric profiles in the central spaxel due to flux differences between the blue and red components. These asymmetric profiles suggest the possibility of dynamic disturbances within these galaxies (Nevin et al. 2016). In this section, we try to figure out the origin of the disturbances.

We search for evidence of external processes (including tidal features, close companion galaxies, as well as gas-star misalignments) that happened in DPGs as well as their controls. To search the tidal features in DPGs and their control sample, we visually inspect the images from Dark Energy Spectroscopic Instrument (DESI) Legacy Imaging Surveys (Dey et al. 2019), which is  $\sim 2$  mag deeper than SDSS. We identify galaxies exhibiting tidal tails, shells, as well as faint stellar streams, and consider these galaxies to have tidal features. We obtain the spectroscopic redshifts of DPGs/controls and their close companions from SDSS single-fiber spectra. The close companions are defined as galaxies within a projected separation of  $r_p \leq 80 h_{70}^{-1}$  kpc and a line-of-sight velocity difference  $\Delta V \leq 300$  km s $^{-1}$  relative to the DPGs/controls (Ellison et al. 2013). We also check the stellar and H $\alpha$  velocity field provided by MaNGA DAP for each galaxy to identify gas-star misaligned galaxies ( $|\text{PA}_{\text{star}} - \text{PA}_{\text{gas}}| > 30^\circ$ ; Zhou et al. 2022). Fig. 12 compares the classifications between double-peaked sample (red histograms) and their control sample (blue histograms). We find that 58.3% (21/36) of the galaxies in our double-peaked sample exhibit evidence of external processes (including tidal features, close companion galaxies, as well as gas-star misalignments), whereas only 27.8% (10/36) of the galaxies in the control sample present these characteristics. This suggests that the origin of double-peaked emission line profiles is associated with external processes.

We compare the stellar population gradients between the DPGs and their controls using continuum spectral indices 4000 Å break ( $D_n4000$ ). Fig. 13 shows the  $D_n4000$  radial gradients for SF (left) and Seyfert/LINER (right) galaxies. The red and blue dots represent the median  $D_n4000$  for the double-peaked sample and control sample, respectively. The error bars are the typical measurement error of  $D_n4000$  at different radii. For the SF galaxies, we find that the  $D_n4000$  gradient of the double-peaked sample is positive, indicating that the double-peaked sample has younger stellar population in the central regions than their outskirts. The  $D_n4000$  gradient of the control sample is negative, indicating older stellar populations in the central regions, as expected for ordinary bulge + disc structure

galaxies. For the Seyfert/LINER galaxies, the double-peaked sample and the control sample have similarly negative  $D_n4000$  gradients. The positive  $D_n4000$  radial gradient for double-peaked SF galaxies can be naturally explained by external processes which trigger gas inflows, leading to a fast centrally concentrated star formation, while shutting down star formation in the outskirts due to the lack of cold gas (Xu et al. 2022). Furthermore, the larger Sérsic index  $n$ , the higher stellar velocity dispersion, and the smaller  $R_e$ , compared to the control sample shown in Fig. 5 can also be explained by the gas inflow picture (Maschmann et al. 2020; Zhou et al. 2022).

## 5 CONCLUSIONS

In this work, we study 36 double-peaked narrow emission-line galaxies selected from 10,010 unique galaxies in MaNGA survey. We use a double Gaussian model to separate the double-peaked profiles for each emission line and perform spatially resolved analyses on the kinematic properties and ionization mechanisms of each Gaussian component. The main findings are summarized below:

(i) Comparing to the control sample, DPGs exhibit a larger Sérsic index  $n$ , higher stellar velocity dispersion, and smaller  $R_e$ .

(ii) In 97.2% (35/36) DPGs, the blue and red components exhibit two distinct velocities and are spatially offset by  $\sim$  kpc scale along the major axes, resulting in significant variations in the flux ratio between the blue and red components along the major axes, while the flux ratio keeps roughly a constant along the minor axes.

(iii) The blue and red components of DPGs exhibit similar distributions in both the value of line-of-sight velocity and the velocity dispersion, indicating that the two components have similar kinematic properties and physical origins.

(iv) 83.3% (30/36) DPGs have both blue and red components located in the same ionization region in the [S II]-BPT diagram, suggesting that the two components are ionized by similar sources. Specifically, 41.7% DPGs have both components classified as Seyfert, while 13.9% are classified as LINER and 27.7% are classified as SF. The remaining 16.7% DPGs have their blue and red components located in different ionization regions.

(v) For the double-peaked SF galaxies, the  $D_n4000$  radial gradient is positive, whereas it is negative for the control sample, indicating that the double-peaked SF galaxies have a younger stellar population in the central regions than their outskirts.

(vi) 58.3% of the DPGs experienced external processes, characterized by tidal features, companion galaxies, as well as gas-star misalignments. This fraction is about twice as much as that of the control sample, suggesting the origin of double-peaked emission line profiles is associated with external processes.

Combining all the observational results listed above, we suggest that double-peaked emission line profiles in 35 out of 36 DPGs primarily originate from rotating discs. The remaining one galaxy shows clear outflow features. 8 out of 35 DPGs show symmetric profiles that indicate undisturbed rotating discs, and the other 27 DPGs exhibit asymmetric profiles, suggesting dynamic disturbances in the rotating discs.

## ACKNOWLEDGEMENTS

YMC acknowledges support from the National Natural Science Foundation of China, NSFC grants 12333002, the China Manned Space Project with NO. CMS-CSST-2025-A08.

Funding for the Sloan Digital Sky Survey IV has been provided by

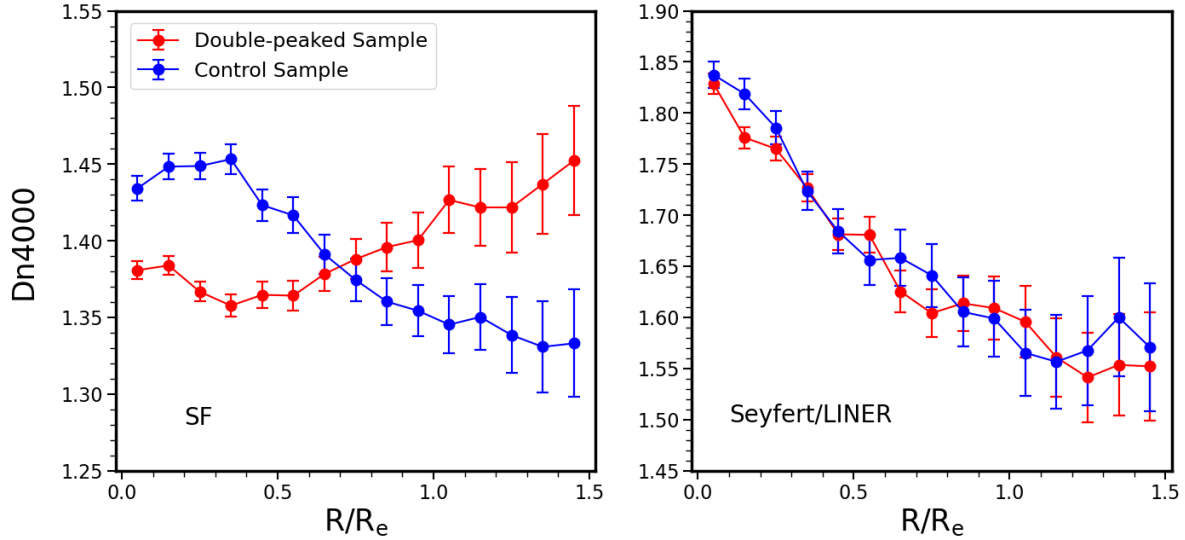


**Figure 13.**  $D_n$ 4000 radial gradients for SF (left) and Seyfert/LINER (right) galaxies. The red and blue dots represent the median  $D_n$ 4000 for the double-peaked sample and control sample, respectively. The error bars are the typical measurement error of  $D_n$ 4000 at different radii.

the Alfred P. Sloan Foundation, the U.S. Department of Energy Office of Science, and the Participating Institutions. SDSS-IV acknowledges support and resources from the Center for High-Performance Computing at the University of Utah. The SDSS website is [www.sdss.org](http://www.sdss.org).

SDSS-IV is managed by the Astrophysical Research Consortium for the Participating Institutions of the SDSS Collaboration including the Brazilian Participation Group, the Carnegie Institution for Science, Carnegie Mellon University, the Chilean Participation Group, the French Participation Group, Harvard-Smithsonian Center for Astrophysics, Instituto de Astrofísica de Canarias, The Johns Hopkins University, Kavli Institute for the Physics and Mathematics of the Universe (IPMU) / University of Tokyo, Lawrence Berkeley National Laboratory, Leibniz Institut für Astrophysik Potsdam (AIP), Max-Planck-Institut für Astronomie (MPIA Heidelberg), Max-Planck-Institut für Astrophysik (MPA Garching), Max-Planck-Institut für Extraterrestrische Physik (MPE), National Astronomical Observatories of China, New Mexico State University, New York University, University of Notre Dame, Observatório Nacional / MCTI, The Ohio State University, Pennsylvania State University, Shanghai Astronomical Observatory, United Kingdom Participation Group, Universidad Nacional Autónoma de México, University of Arizona, University of Colorado Boulder, University of Oxford, University of Portsmouth, University of Utah, University of Virginia, University of Washington, University of Wisconsin, Vanderbilt University, and Yale University.

## DATA AVAILABILITY

The data underlying this article will be shared on reasonable request to the corresponding author.

## REFERENCES

Abazajian K. N., et al., 2009, *ApJS*, **182**, 543  
 Abdurro'uf et al., 2022, *ApJS*, **259**, 35  
 Albán M., Wylezalek D., 2023, *A&A*, **674**, A85  
 Avery C. R., et al., 2021, *MNRAS*, **503**, 5134  
 Baldwin J. A., Phillips M. M., Terlevich R., 1981, *PASP*, **93**, 5  
 Bao M., Chen Y.-m., Yuan Q.-r., Shi Y., Bizyaev D., Yu X.-l., Gu Q.-s., Yu Y., 2019, *MNRAS*, **490**, 3830  
 Bao M., et al., 2021, *MNRAS*, **505**, 191  
 Belfiore F., et al., 2016, *MNRAS*, **461**, 3111  
 Benedetti J. P. V., et al., 2024, *MNRAS*, **534**, 400  
 Blanton M. R., Kazin E., Muna D., Weaver B. A., Price-Whelan A., 2011, *AJ*, **142**, 31  
 Blanton M. R., et al., 2017, *AJ*, **154**, 28  
 Blecha L., Loeb A., Narayan R., 2013, *MNRAS*, **429**, 2594  
 Bundy K., et al., 2015, *ApJ*, **798**, 7  
 Cappellari M., Emsellem E., 2004, *PASP*, **116**, 138  
 Chen Y.-M., Tremonti C. A., Heckman T. M., Kauffmann G., Weiner B. J., Brinchmann J., Wang J., 2010, *AJ*, **140**, 445  
 Comerford J. M., Gerke B. F., Stern D., Cooper M. C., Weiner B. J., Newman J. A., Madsen K., Barrows R. S., 2012, *ApJ*, **753**, 42  
 Comerford J. M., Pooley D., Barrows R. S., Greene J. E., Zakamska N. L., Madejski G. M., Cooper M. C., 2015, *ApJ*, **806**, 219  
 Comerford J. M., Nevin R., Stemo A., Müller-Sánchez F., Barrows R. S., Cooper M. C., Newman J. A., 2018, *ApJ*, **867**, 66  
 Dey A., et al., 2019, *AJ*, **157**, 168  
 Diniz S. I. F., Pastoriza M. G., Hernandez-Jimenez J. A., Riffel R., Ricci T. V., Steiner J. E., Riffel R. A., 2017, *MNRAS*, **470**, 1703  
 Drory N., et al., 2015, *AJ*, **149**, 77  
 Ellison S. L., Mendel J. T., Scudder J. M., Patton D. R., Palmer M. J. D., 2013, *MNRAS*, **430**, 3128  
 Fabian A. C., 2012, *ARA&A*, **50**, 455  
 Fischer T. C., et al., 2017, *ApJ*, **834**, 30  
 Fischer J. L., Domínguez Sánchez H., Bernardi M., 2019, *MNRAS*, **483**, 2057  
 Fu H., Yan L., Myers A. D., Stockton A., Djorgovski S. G., Aldering G., Rich J. A., 2012, *ApJ*, **745**, 67  
 Fu Y., Cappellari M., Mao S., Lu S., Zhu K., Li R., 2023, *MNRAS*, **524**, 5827  
 Greene J. E., Ho L. C., 2005, *ApJ*, **627**, 721  
 Greene J. E., Zakamska N. L., Ho L. C., Barth A. J., 2011, *ApJ*, **732**, 9  
 Gunn J. E., et al., 2006, *AJ*, **131**, 2332  
 Heckman T. M., 1980, *A&A*, **87**, 152  
 Heckman T. M., Miley G. K., van Breugel W. J. M., Butcher H. R., 1981, *ApJ*, **247**, 403  
 Heckman T. M., Miley G. K., Green R. F., 1984, *ApJ*, **281**, 525  
 Heckman T. M., Armus L., Miley G. K., 1990, *ApJS*, **74**, 833  
 Karouzos M., Woo J.-H., Bae H.-J., 2016, *ApJ*, **819**, 148  
 Kewley L. J., Dopita M. A., Sutherland R. S., Heisler C. A., Trevena J., 2001,

ApJ, 556, 121

Kewley L. J., Groves B., Kauffmann G., Heckman T., 2006, MNRAS, 372, 961

Kewley L. J., Nicholls D. C., Sutherland R. S., 2019, ARA&A, 57, 511

Krajnović D., Cappellari M., de Zeeuw P. T., Copin Y., 2006, MNRAS, 366, 787

Law D. R., et al., 2015, AJ, 150, 19

Law D. R., et al., 2016, AJ, 152, 83

Liddle A. R., 2007, MNRAS, 377, L74

Liu X., Shen Y., Strauss M. A., Greene J. E., 2010, ApJ, 708, 427

Maschmann D., Melchior A.-L., Mamon G. A., Chilingarian I. V., Katkov I. Y., 2020, A&A, 641, A171

Maschmann D., Halle A., Melchior A.-L., Combes F., Chilingarian I. V., 2023, A&A, 670, A46

Mazzilli Ciraulo B., Melchior A.-L., Maschmann D., Katkov I. Y., Halle A., Combes F., Gelfand J. D., Al Yazeedi A., 2021, A&A, 653, A47

Müller-Sánchez F., Comerford J. M., Nevin R., Barrows R. S., Cooper M. C., Greene J. E., 2015, ApJ, 813, 103

Nevin R., Comerford J., Müller-Sánchez F., Barrows R., Cooper M., 2016, ApJ, 832, 67

Nevin R., Comerford J. M., Müller-Sánchez F., Barrows R., Cooper M. C., 2018, MNRAS, 473, 2160

Qiu J., Shen S., Feng S., Chen Y., Chang R., Zhao Q., Zeng Q., 2024, ApJ, 976, 15

Qiu J., Shen S., Chang R., Zhao Q., Zeng Q., 2025, arXiv e-prints, p. arXiv:2507.21512

Raimundo S. I., Malkan M., Vestergaard M., 2023, Nature Astronomy, 7, 463

Reines A. E., Greene J. E., Geha M., 2013, ApJ, 775, 116

Rembold S. B., et al., 2024, MNRAS, 527, 6722

Riffel R., et al., 2023, MNRAS, 524, 5640

Russell H. R., et al., 2019, MNRAS, 490, 3025

Sakamoto K., Aalto S., Combes F., Evans A., Peck A., 2014, ApJ, 797, 90

Sánchez S. F., 2020, ARA&A, 58, 99

Sargent W. L. W., 1972, ApJ, 173, 7

Sarzi M., et al., 2010, MNRAS, 402, 2187

Schwarz G., 1978, Annals of Statistics, 6, 461

Shen Y., Liu X., Greene J. E., Strauss M. A., 2011, ApJ, 735, 48

Smee S. A., et al., 2013, AJ, 146, 32

Smith K. L., Shields G. A., Bonning E. W., McMullen C. C., Rosario D. J., Salviander S., 2010, ApJ, 716, 866

Smith K. L., Shields G. A., Salviander S., Stevens A. C., Rosario D. J., 2012, ApJ, 752, 63

Stasińska G., et al., 2008, MNRAS, 391, L29

Swinbank A. M., et al., 2019, MNRAS, 487, 381

Veilleux S., Maiolino R., Bolatto A. D., Aalto S., 2020, A&ARv, 28, 2

Virtanen P., et al., 2020, Nature Methods, 17, 261

Wake D. A., et al., 2017, AJ, 154, 86

Wang J.-M., Chen Y.-M., Hu C., Mao W.-M., Zhang S., Bian W.-H., 2009, ApJ, 705, L76

Wang M. X., et al., 2019, MNRAS, 482, 1889

Westfall K. B., et al., 2019, AJ, 158, 231

Woo J.-H., Bae H.-J., Son D., Karouzos M., 2016, ApJ, 817, 108

Xu H., et al., 2022, MNRAS, 511, 4685

Yan R., et al., 2019, ApJ, 883, 175

Zhou Y., et al., 2022, MNRAS, 515, 5081

Zhou Z.-J., Chen Y.-M., Guan R.-Q., Shi Y., Gu Q.-S., Bizyaev D., 2024, MNRAS, 531, 2462

This paper has been typeset from a Te<sub>X</sub>/La<sub>T</sub>E<sub>X</sub> file prepared by the author.